

Optimal control of eye-movements during visual search

A.Y.Vasilyev

Queen Mary University of London, Mile End Road, E1 4NS

Abstract

We study the problem of optimal oculomotor control during the execution of visual search tasks. We introduce a computational model of human eye movements, which takes into account various constraints of the human visual and oculomotor systems. In the model, the choice of the subsequent fixation location is posed as a problem of stochastic optimal control, which relies on reinforcement learning methods. We show that if biological constraints are taken into account, the trajectories simulated under learned policy share both basic statistical properties and scaling behaviour with human eye movements. We validated our model simulations with human psychophysical eye-tracking experiments.

Keywords: scaling in biology, visual search, reinforcement learning, multifractal analysis

1. Introduction

The human oculomotor system performs millions of eye-movements per day during the execution of different behavior goals. In order to find the details on a visual scene related to the tasks, humans direct foveal vision to the most informative locations via saccades - high velocity conjugate gaze shifts. Saccades are followed by a visual fixation, during which the human oculomotor system generates fixational eye movements involuntarily. Despite the remarkable achievements in the modeling of fixational eye movements and interpretation of their fundamental properties [1, 2, 3], there is no comprehensive generic model of fixation selection [4, 5, 6], which takes into account the underlying mechanisms of visual attention [5, 7, 8] and qualitatively describes the statistical properties of saccadic eye-movements during execution of visual tasks [9, 10, 11, 12].

Previously the problem of fixation selection was studied in the framework of control models of eye movements [13, 11, 9]. In control models the observer gathers information about the world during

each fixation, integrates information over all fixations and makes an optimal choice of the next location to fixate. The choice of next location is governed by policy of gaze allocation. It was shown that the policy based on information maximization criteria [9] generates trajectories that share basic statistical properties with human eye movements. In this research we set the goal to develop the control model of fixation selection that is capable of interpreting the scaling behaviour of human eye-movements [10, 14, 12, 15] and provides a human level of performance to a computational agent.

In contrast to previous research on control models, we take into account inherent uncertainty of human oculomotor system and duration of saccadic eye movements. It's well known that any motor action of human is executed with random error, which increases with movement magnitude [16, 17]. Despite oculomotor system having developed a correction mechanism for saccade errors [18], these result in inevitable temporal costs. Furthermore, the duration of saccades is empirically correlated with their magnitude as well [19]. These factors result in sit-

uations where the observer has to choose between more informative remote (and more risky) locations and nearby, (but less informative) ones. We show that if these constraints are taken into consideration, the trajectories simulated under learned policy share both basic statistical properties and scaling behavior with human eye movements, which is not achievable with conventional infomax model [9].

On the basis of our results we argue that we have made the following contribution:

- Formulation of biologically plausible model of gaze allocation in human observer from the point of view of stochastic optimal control. Representation of the model in the form of partially observable Markov decision process (PO-MDP) and proposal of heuristic policy.
- Development of robust and high performance algorithms of simulation of PO-MDP. Implementation of reinforcement learning algorithms of policy optimization and numerical estimation of optimal policy of gaze allocation.
- Comprehensive statistical analysis of simulated trajectories and data from our psycho-physical experiments. The policy, which is learned with policy gradient REINFORCE algorithm, shows the highest level of statistical similarity with human eye-movements. In our experiments we discovered the dependency of mean saccade length and q-order Hurst exponent on visibility of target, which was explained by our model.

2. Model of ideal observer

In this section we formulate the model of ideal observer, which aims to localize the single target object on the stationary 2D image.

2.1. World state

In the beginning of each episode the target object appears randomly at the one of L possible locations. We assume that the target is placed on background noise or surrounded by distractors, which are placed on vacant locations. The world state S_n is represented as a tuple:

$$S_n = (l_0, A_n, t_n) \quad (1)$$

where l_0 is location of target on the image and A_n is gaze fixation location that changes with the number of step n , and t_n is time passed from the start of a trial and the step n .

If observer fixates the gaze on location of target $A_n = l_0$, the visual task is considered to be accomplished. This formulation of terminal state reflects the necessity to foveate the target in order to extract as much information about its identity and details as possible.

2.2. Belief state

The decision making of observer is modelled as PO-MDP with belief state p_n - probability distribution function of target location given all observations received up to step n . The decision of which location to fixate next, D_n , is made on each step of PO-MDP according to policy of gaze allocation $\mu : D_n = \mu(p_{n-1})$. After making the decision, the coordinates of the next fixation location are defined by execution function: $A_n = \alpha(D_n)$. After relocation of gaze to A_n observer receives the observation vector $\mathbf{W}^n = (W_1^n, \dots, W_L^n)$, whose elements represent the perceptual evidence that the target is at corresponding locations. The probability distribution function on the next step is computed via Bayes theorem:

$$p_n(l) = \frac{p_{n-1}(l)p(\mathbf{W}^n|l, A_n)}{\sum_k p_{n-1}(k)p(\mathbf{W}^n|k, A_n)} \quad (2)$$

where l is index of location and $p(\mathbf{W}^n|l, A_n)$ is the observation model. In order to take into account the uncertainty of processing of perceptual information within the neural circuits of the observer, we follow the “noisy observation” paradigm [9]. In this paradigm the observation model $p(\mathbf{W}^n|l, A_n)$ reflects the presence of observer’s internal sources of inefficiency, such as physical neural noise on all stages of information processing. According to the perceptual model [11] observation \mathbf{W}^n may be represented as a random variable with Gaussian distribution with mean that depends on location of the center of target on the lattice:

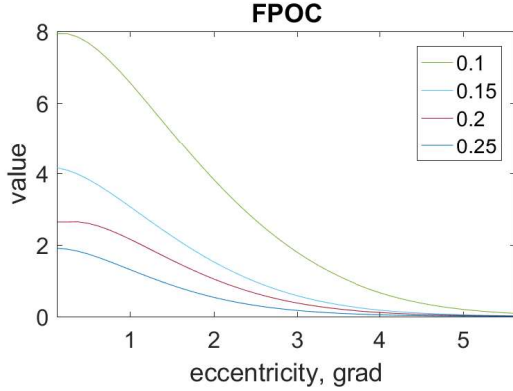


Figure 1: Fovea-Peripheral Operating Characteristic was calculated for several values of rms contrast of background noise: $e_n \in (0.1, 0.15, 0.2, 0.25)$ and single value of RMS contrast of target $e_t = 0.2$. Signal to noise ratio has a peak at fovea and decreases rapidly with eccentricity.

$$p(\mathbf{W}^n | l, A_n) = \prod_l p(W_l^n | A_n) = \\ = \prod_l N(W_l^n; \delta_{l, l_0} - \frac{1}{2}, \frac{1}{F(\|l - A_n\|)}) \quad (3)$$

where $\delta_{i,j}$ is Kronecker delta, $N(x, \mu, \nu)$ is value of Gaussian function with mean μ and variance ν for argument x ; $\|l - A_n\|$ is Euclidian distance between locations l and current fixation A_n , and F is a Fovea-Peripheral Operating Characteristic (FPOC) [13]. FPOC is function that represents dependence of signal to noise ration on eccentricity. Figure (1) demonstrates FPOC calculated for several values of RMS contrast of background 1/f noise: $e_n \in (0.1, 0.15, 0.2, 0.25)$ and single value of RMS contrast of target $e_t = 0.2$. The calculation are based on analytical expressions and data from [11]. Signal to noise ratio has a peak at fovea and decreases rapidly with eccentricity. In this research we consider only the case of rotationally symmetric FPOC.

2.3. Execution of saccades

The decision where to fixate next is determined by policy of gaze allocation $D_n = \mu(p_{n-1})$. After de-

cision making oculomotor system performs saccadic eye-movement to the next location defined as:

$$A_n = \alpha(D_n) = D_n + J_n \quad (4)$$

where J_{n+1} is Gaussian-distributed random error with zero mean and variance ν defined in [17]:

$$\nu = \zeta_0 + \zeta_1 \|D_n - A_{n-1}\| \quad (5)$$

The error of saccade execution is proportional to intended saccade amplitude $\|D_n - A_{n-1}\|$ given in degrees, the value of parameters: $\zeta_0 = 0.87^\circ$, $\zeta_1 = 0.084^\circ/\text{deg}$. We assume that decision making process can easily adapt to the systematic saccade range error mentioned in [17].

The next step of MDP starts after transition to new location A_n . The process is repeated until arrival to terminal state $A_n = l_0$.

2.4. Duration of steps

After each consequent step the time variable t of world state (1) is updated in deterministic way:

$$t_{n+1} \leftarrow t_n + \Theta(n) \quad (6)$$

where $\Theta(n)$ is duration of step n . The duration of time step $\Theta(n)$ is considered as a total time, which is required for relocation of the gaze and extraction of visual information from new location. Therefore, we consider $\Theta(n)$ as a sum of fixation $\Theta_{fix}(n)$ and saccade $\Theta_{sac}(n)$ durations. According to the literature, both of these time intervals are empirically correlated with magnitude of saccade preceding the fixation [19, 20, 21]. The duration of saccadic eye-movements $\Theta_{sac}(n)$ in range of magnitudes from 1.5° to 30° is possible to approximate as [22]:

$$\Theta_{sac}(n) = \tau_{sac} \|A_n - A_{n-1}\|^{0.4} \quad (7)$$

where $\tau_{sac} = 0.021s \cdot \text{deg}^{-0.4}$. Besides the magnitude of saccade, fixation duration $\Theta_{fix}(n)$ is influenced by various factors as discriminability of the target [23], its complexity and the visual task of observer [21][24]. However, if the observer is correctly informed about the targets' properties before the task execution and performs the visual task without any interruptions, the contribution of these factors to

fixation duration (with exception of magnitude) is constant during each trial. The eye-tracking experiments with fixations tasks [21][20, 21, 25] found that dependence of fixation duration on saccade amplitude is linear:

$$\Theta_{fix}(n) = \|A_n - A_{n-1}\| \tau_{fix} + \Theta_{0,fix} \quad (8)$$

with the slope τ_{fix} varying from 2.7 to 6 milliseconds per degree. The constant $\Theta_{0,fix} = 250ms$ is intercept, averaged from values from eye-tracking data [26][27]. Finally, the duration of step n is:

$$\Theta(n) = \Theta_{sac}(n) + \Theta_{fix}(n) \quad (9)$$

2.5. Value function

Given the initial probability density function p_0 we define the cost function for policy μ as expectation of random variable L :

$$V_\mu(p_0) = E [L|\mu, p_0] \quad (10)$$

The random variable L denotes cost and is defined by:

$$L \equiv c \sum_{n=0}^N \Theta(n) = ct_N \quad (11)$$

where N is total number of steps in episode, and c is a time cost constant.

Formulation of value function in real time positions this study separately from previous works [28, 11, 13]. We show below, that the policy μ optimized for value function with reward defined in (11) generates the saccadic eye-movements with statistical characteristics close to human ones.

3. Policy of gaze allocation

3.1. Infomax approach

In this section we describe two heuristic policies related to the model of Entropy Limit Minimization searcher [9]. We define information gain on step $n+1$ as: $\Delta I(n+1) = H(p_n) - H(p_{n+1})$, where $H(\cdot)$ is Shannon entropy. The heuristic policy π_0 is defined as a policy which chooses such decision D_{n+1} that maximizes the expected information gain $\Delta I(n+1)$:

$$\pi_0(p_n) = D_{n+1} = \arg \max_D [E [\Delta I(n+1)]] \quad (12)$$

The term $E [\Delta I(n+1)]$ is calculated analytically in [9] for the case of saccadic eye-movement without uncertainty ($A_{n+1} \equiv D_{n+1}$):

$$E [\Delta I(n+1)] = \frac{1}{2} (p_n * F) (A_{n+1}) \quad (13)$$

where sign $*$ denotes convolution operator, and F is FPOC represented as 2D function: $F(A) \equiv F(\|A\|)$. The expression (13) gives only approximate value of expected information gain in the case of stochastic saccadic placement (4).

The figure 2 demonstrates the decision making process, which corresponds to policy π_0 . The colour map (left) represents the function of expected information gain (equation (13)). The blue cross corresponds to location of the current fixation on the step n . The observer makes decision to fixate at location defined by policy: $D_{n+1} = \pi_0(p_n)$. This decision results in saccadic eye-movements to location $A_{n+1} = \alpha(D_{n+1})$ marked by green cross. After receiving observation at step $n+1$, observer updates belief state and evaluate information gain for the next decision. In this particular situation, the target was absent at the vicinity of A_{n+1} , and observation resulted in decline of probability p_{n+1} in the area around the green cross (figure 2 right). This area is effectively inhibited from subsequent fixations due to low probability. The size of this area is defined by values of FPOC ($e_t = 0.2$, $e_n = 0.1$ in this case). Below in the text we call the policy π_0 “infomax greedy”.

The trajectories generated with this kind of policy match basic properties of human eye movements [9]. However, the policy (13) doesn't consider the correlation between magnitude of saccades and the durations of steps of MDP. We show later that the policy π_0 is inferior to the policy that optimizes the expected rate of information gain $E [\Delta I(n+1)/\Theta(n+1)]$:

$$\pi_1(p_n) = D_{n+1} = \arg \max_D [E [\Delta I(n+1)/\Theta(n+1)]] \quad (14)$$

Using the expression for $\Delta I(n+1)$ (13), for deterministic saccadic placement ($A_{n+1} \equiv D_{n+1}$):

$$E[\Delta I(n+1)/\Theta(n+1)] = E\left[\frac{\frac{1}{2}(p_n * F)(D_{n+1})}{\Theta(n+1)}\right] \quad (15)$$

The final expression for policy π_1 is:

$$\pi_1(p_n) = \arg \max_{D_{n+1}} \left[\frac{p_n * F}{\Theta(n+1)} (D_{n+1}) \right] \quad (16)$$

Below in the text the policy π_1 is called “info-max rate”. The performance of these two heuristic policies will be compared with performance of policy learned with reinforcement learning algorithms in the section Appendix A.3.1.

3.2. Optimal policy estimation

In order to find optimal policy of gaze allocation we use the reinforcement learning algorithms of policy gradient. Policy gradient methods [29, 30] are reasonable to use in the optimization problem with high dimensional state-action space. We approach the problem(23) with policy gradient parameter-exploring (PGPE) [31] algorithm and with algorithm for PO-MDP problems adopted from [29] (Episodic REINFORCE with optimal baseline).

We start with representation of the stochastic policy μ in the form of softmax function [32]:

$$\mu(D, p) = \frac{\exp(f(D, p)/\lambda)}{\sum_l \exp(f(l, p)/\lambda)} \quad (17)$$

where $f(D, p)$ is the function of expected reward gain after making the decision D with the belief state p , and λ is the “temperature” parameter, which defines the variance of softmax function. In the case $\lambda \rightarrow \infty$ we have uniform distribution among decisions, and in the opposite case $\lambda \rightarrow 0$, this stochastic policy is identical to deterministic one:

$$\pi(p) = \arg \max_D f(D, p) \quad (18)$$

Due to this property, the function (17) is called softmax function, and it is commonly used to avoid

singularity of derivative of (18). The goal of optimization process is to find the stochastic policy $\mu(D, p)$, which optimizes the value function (10). In this study we limit the search of $f(D, p)$ to linear transformations [32] of belief state p :

$$f(D, p) \equiv \sum_l K(l, D)p(l) \quad (19)$$

In general, we assume that process of visual search is characterised by shift-rotational invariance [13]. The coefficients in the set of dynamic equations (3,4,9) are unaltered under any distance preserving transformations. The last dynamic equation, which is the policy of gaze allocation (17), should be shift-rotational invariant as well. The policy (17) is determined by function of expected reward $f(D, p)$. Therefore, the coefficients $K(l, D)$ from (19) should be shift-rotational invariant. Also, the function of expected reward should be computed taking into account the current location of the observer. The most general form of this function is: $f(D, p) = \sum_l K(\|D - l\|, \|D - A_n\|)p(l)$. The softmax policy (17) for this function of expected reward is:

$$\mu(D_{n+1}, p_n) =$$

$$= \frac{\exp\left(\frac{1}{\lambda} \sum_l p_n(l) K(\|D_{n+1} - l\|, \|D_{n+1} - A_n\|)\right)}{N} \quad (20)$$

where N denotes the normalization term. Together with the set of equations (3,4,9), this form of policy keeps the evolution of system invariant under any distance-preserving transformation. The convolution of probability distribution with the kernel function $K(x, y)$ in general form 20 is difficult to optimize, and the problem can be effectively solved only in separable approximation:

$$\begin{aligned} & K(\|D_{n+1} - A_n\|, \|D_{n+1} - x\|) \\ & \approx R(\|D_{n+1} - A_n\|) S(\|D_{n+1} - x\|) \end{aligned} \quad (21)$$

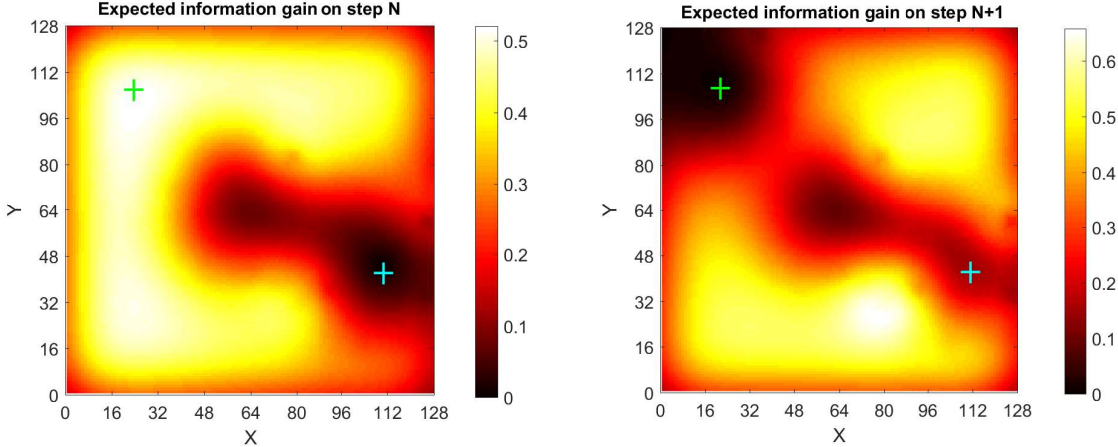


Figure 2: The decision making process under infomax greedy policy π_0 [9]. The colour map (left) represents the function of expected information gain (equation (13)). The blue cross corresponds to location of the current fixation on the step n . The observer makes decision to fixate at location defined by policy: $D_{n+1} = \pi_0(p_n)$. This decision results in saccadic eye-movement to location $A_{n+1} = \alpha(D_{n+1})$ marked by green cross. After receiving observation at step $n+1$, observer updates belief state and evaluates information gain for the next decision. In this particular situation, the target is absent in vicinity of A_{n+1} , and the observation resulted in decline of probability p_{n+1} in the area around fixation (green cross). This area is effectively inhibited from subsequent fixations due to low probability p_{n+1} . The size of this area is defined by values of FPOC (in this case $e_t = 0.2$, $e_n = 0.1$).

We call R and S the radial and smoothing functions correspondingly. The first one characterizes the dependence of expected reward on intended saccade length. The motivation behind the introduction of radial function R are both growing uncertainty of fixation placement (4) and duration of the step (9) with the length of saccade. We assume that radial function R equals zero outside interval $[a_{min}, a_{max}]$, where a_{min} and a_{max} are minimal and maximal saccade length correspondingly. The minimal saccade length $a_{min} = 1deg$ [33] is chosen as a magnitude of the shortest possible voluntary movement. The maximal saccade length $a_{max} = \sqrt{2} \cdot 15deg$ is equal to the length of diagonal of stimulus image in our experiments. The smoothing function S describes the relative contribution of surrounding locations to reward. The smoothing function has the same role as term F (see eq. (13)) in definition of information maximization policy π_0 , and it basically defines how meaningful the certain location is without consideration of time costs of relocation.

The form of policy (20) in separable approximation is:

$$\mu(D_{n+1}, p_n) =$$

$$= \frac{\exp\left(\frac{1}{\lambda} R(\|D_{n+1} - A_n\|) (p_n * S)(D_{n+1})\right)}{N} \quad (22)$$

which is used in simulation of trajectories and training phase. Two heuristic policies presented in section 3.1 are both special cases of general form of policy (22).

Our task, therefore, is reduced to the search of function $K(x, y)$ (21) and temperature parameter λ , which correspond to the policy that optimizes the cost function V_μ :

$$(K^*, \lambda^*) = \arg \min_{K, \lambda} V_{\mu(K, \lambda)}(S_0) \quad (23)$$

for any starting world state $\forall S_0 : S_0 \in B$, where B is set of initial world states. The policy $\mu(K^*, \lambda^*)$

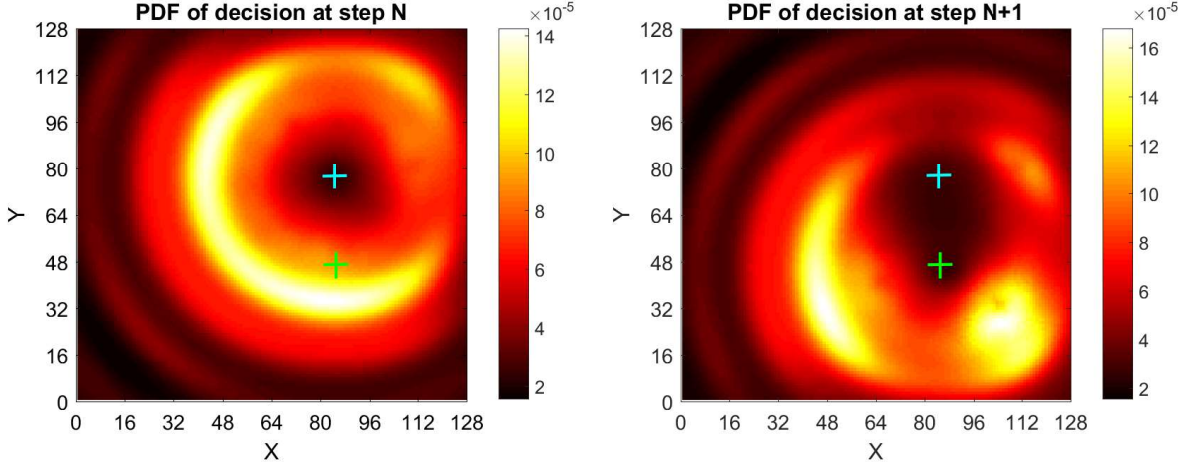


Figure 3: The decision making process under policy learned for FPOC corresponding to conditions $e_t = 0.2$, $e_n = 0.2$. At the step n observer fixates the location marked by blue cross. The policy μ defines probability density function of decision D where to fixate next (22). Observer chooses the decision D_{n+1} according to policy, which results in saccadic eye-movement to location $A_{n+1} = \alpha(D_{n+1})$ (green cross). As well as in the case of dynamics under heuristic policy π_0 previously visited locations are inhibited from subsequent fixations. Note that movements to remote locations are inhibited by radial function. This results in co-directed short movements, which are also characteristic of human observer (see figure C.16)

is called optimal policy of gaze allocation. We numerically estimate the optimal policy with algorithm named “REINFORCE with optimal baseline” [34] according to the procedure described in Appendix A. The performance of REINFORCE was compared with the one of optimization algorithm named “policy gradient parameter exploration” (PGPE) adopted from [31]. The algorithm of REINFORCE with optimal baseline belongs to the class of likelihood ratio methods, whereas PGPE is related to finite difference methods. Despite the distinction between these two approaches, both algorithms give close estimation of optimal policy Appendix A.3.1. We simulated trajectories for data analysis in section 5 using the solution provided by REINFORCE due it’s better performance comparing to PGPE.

Figure 3 demonstrates the decision making process under policy μ learned for FPOC corresponding to conditions $e_t = 0.2$, $e_n = 0.2$ (see figure A.15 for it’s kernel function). At the step n observer fixates the location marked by blue cross. The policy μ defines probability density function of deci-

sion D where to fixate next (22). Observer chooses the decision $D_{n+1} = \mu(p_n)$, which results in saccadic eye-movement to location $A_{n+1} = \alpha(D_{n+1})$ (green cross). As well as in the case of dynamics under heuristic policy π_0 , previously visited locations are inhibited from subsequent fixations. Note that movements to remote locations are inhibited by radial function. This results in co-directed short movements, which are also characteristic of human observer (see figure C.16).

4. Psychophysical experiments

We set a goal to reproduce an eye tracking experiment described in [11]. In this section we provide the description of psychophysical experiments.

4.1. Participants

The group of nine patients with normal to corrected-to-normal vision participated in the experiment. The group included five naive postgraduate students (age 30 ± 10 , 3 females and 2 males) from school of Biological and Chemical Sciences and

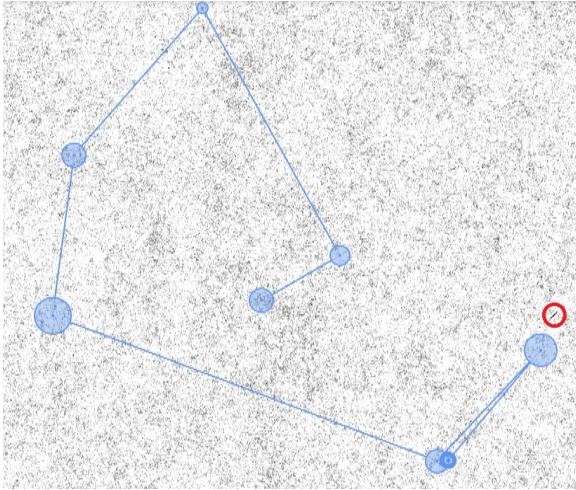


Figure 4: The stimulus image in psycho-physical experiment: target object circled by red surrounded by $1/f$ noise. The scan-path is shown with blue lines and circles, which radii denote the durations of fixations. The scan-path starts at the center of image, which is controlled by presenting the single high-contrast stimulus (black dot with radius 0.25 deg) in the center of display before each trial.

four members (age 30 ± 10 , 4 males) of Visual Perception Lab. These two groups are called “naive observers” and “trained observers” correspondingly. The group of trained observers was aware of experimental settings and passed 10 minutes of training sessions with various experimental conditions. The group of naive observers passed only one practice session, which last around 2 min and had only explanatory purpose. The experiments were approved by the ethics committee of Queen Mary University of London and informed consent was obtained.

4.2. Equipment

We used DELL P2210 22" LCD monitor (resolution 1680×1050 , refresh rate 60 Hz) driven by a Dell Precision laptop for all experiments. Eye movements of the right eye were registered using Eye Tracker device SMI-500 with sampling frequency of 120 Hz. The Eye tracker device was mounted on the monitor. Matlab Psychtoolbox was used to run experiments and generate stimulus images.

4.3. Stimulus and procedure

Participants set in front of monitor with their heads fixed with a chin rest at a distance of 110 cm from monitor. The monitor subtended a visual angle of $21 \times 16 \text{ deg}$. Each participant was shown the examples of stimulus image before experiments and was instructed to fixate the target object as fast as possible and to press the certain button on keyboard to finish the trial. All nine participants completed one practice session with 40 trials before experiment.

The stimuli were static images generated before each session according to description from original experiment [11]. The $1/f$ noise was a square region on the screen, which spans visual angle of $15 \times 15 \text{ deg}$. The target was 6 deg^{-1} sine grating framed by symmetric raised cosine. It appeared randomly at any possible location on the stimuli image within square region. The experiments were provided for one level of rms contrast of target $e_t = 0.2$ and several levels of $1/f$ noise rms contrast $e_n \in (0.1, 0.15, 0.2, 0.25)$. Figure 4 demonstrates the typical stimulus image and scan-path measured with eye-tracker.

Participants completed four experimental sessions with 40 trials. The experimental session started after inbuilt nine-point grid calibration of eye-tracking device. Participants were given 3 minutes of rest between sessions. One of 40 stimuli images was shown at the beginning of each trial. The participants are assumed to perform visual search task, which is finished by pressing the “END” button. In our experimental settings the signal from participants was blocked for 300 ms from the start of each trial. If the gaze position measured by eye tracking device is in vicinity of 2deg around location of target at the moment participant presses the “END” button, the task is considered successful. After completion of each trial the central fixation cross was shown for 500 ms, then the next trial started and new stimulus image was shown to participants.

5. Basic properties of trajectories

In this section we discuss the statistical properties of trajectories generated with learned policy μ and

heuristic policies π_0 and π_1 , including geometrical persistence and multifractal spectrum. Simulations were performed on the grid with size 128×128 that corresponds to visual field with size of $15 \times 15 \text{deg}$ in psychophysical experiment. The qualitative analysis of eye-movements trajectories is presented in Appendix C.

5.1. Performance

Although this computational model was not designed for exact prediction of response time of human observer, it demonstrates high level of consistency in performance of visual task execution with human. Performance was measured as an average time to reach target (mean completion time) and as percentage of correct fixations on target's location on an N-Alternative Forced Choice task (N-AFC). Unsuccessful trials from psychophysical experiments were excluded from consideration.

Figure 5 (left) demonstrates the percentage of correct fixations on target location for experimental conditions: $e_n = 0.2$, $e_t = 0.2$. The learned policy outperforms two heuristics both in mean completion time and percentage of correct responses in N-AFC task. The dependence of mean completion time on visibility of target for trained observer can be correctly described by learned policy (see (5) right). However, due to significant difference of mean completion time between the groups, we can't make conclusion about the implementation of certain policy in humans solely on the basis of performance.

5.2. Amplitude distribution

The simulated eye movement trajectories under policies π_0, π_1 and μ share several basic statistical properties with human eye-movements. The Figure 6 shows the length distribution of saccadic events. Simulations were performed with FPOC corresponding to experimental conditions: $e_n = 0.2$, $e_t = 0.2$.

The distributions for all policies and human observer exhibit an ascent between 0deg and maximum around 2deg . The difference in behaviour of distributions starts from 4deg . In this experimental conditions the share of saccades of human observer with

length larger than 4deg is 18%, whereas these values for π_0 and π_1 are 38% and 14% correspondingly. The length distribution for π_0 on $[4.0^\circ, 14.0^\circ]$ forms "stability interval" that was observed in earlier work [11], and we found that it's length increases linearly with the grid size. The reason behind this is uniform radial ranking of policy π_0 for all locations due to constant radial function (13). The decline of probability starts only at distance compared to the size of visual field.

On the other hand the length distributions of trajectories under μ, π_1 are concave on interval $[4.0^\circ, 14.0^\circ]$, which is also a characteristic for human eye-movement [35, 36]. The behaviour of radial function of μ reflects non-uniform radial ranking (preference in decision making, see figure (3)) of locations. As a result, remote locations have significantly lower probability to be chosen as the next destination. According to Kolmogorov-Smirnov test for distributions μ_{conv}, π_1, π_0 with distribution for human as a reference, their hypothesis are rejected on levels of α : 0.15, 0.12, 0.08 correspondingly.

The mean length of saccadic eye-movements depends on visibility of target, which was not discussed in earlier works [11]. According to our experiments, the mean length of saccades decreases with e_n , which is consistent with our simulations (see figure 6 right). It's an immediate consequence of decrease of values of FPOC with increase of RMS contrast of noise, which is illustrated on figure 1. The amplitude of signal exceeds the amplitude of noise within the circle area with radius r that satisfies the condition $F(r) = 1$ (we call this radius "width of FPOC"). This circle area is effectively inhibited from subsequent fixations (see figures (2) and (3)), because information is already gathered with sufficient level of confidence. The radius r is correlated with mean length of saccadic events both for human eye-movements and simulated trajectories under learned policy. ($R^2 = 0.86$).

5.3. Geometrical persistence

In this chapter we analyze the distribution of the directional angle θ_d (this notation was introduced in [10]) of human saccadic eye-movements and simulated trajectories. The directional angle is the an-

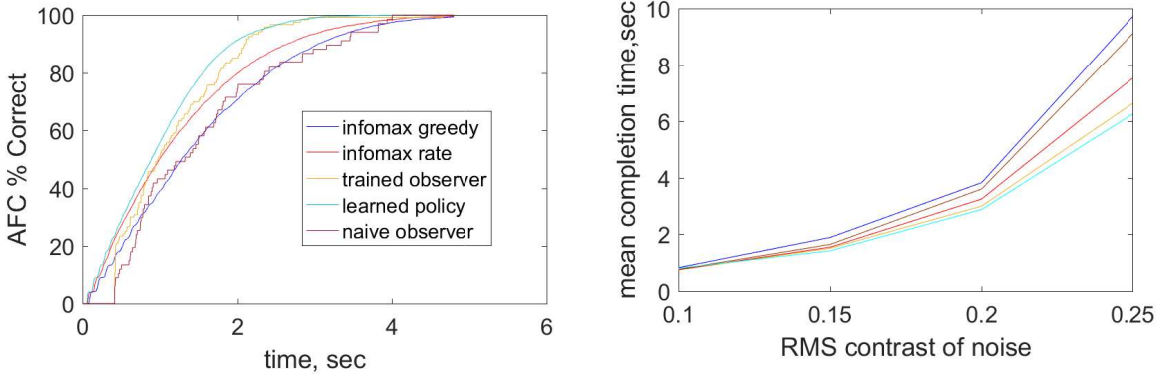


Figure 5: Performance of human observers and simulated agents. The learned policy outperforms two heuristics both in mean completion time and percentage of correct responses in N-AFC task (left). The dependence of mean completion time (right) for learned policy resembles the one for human observer (see (5) right).

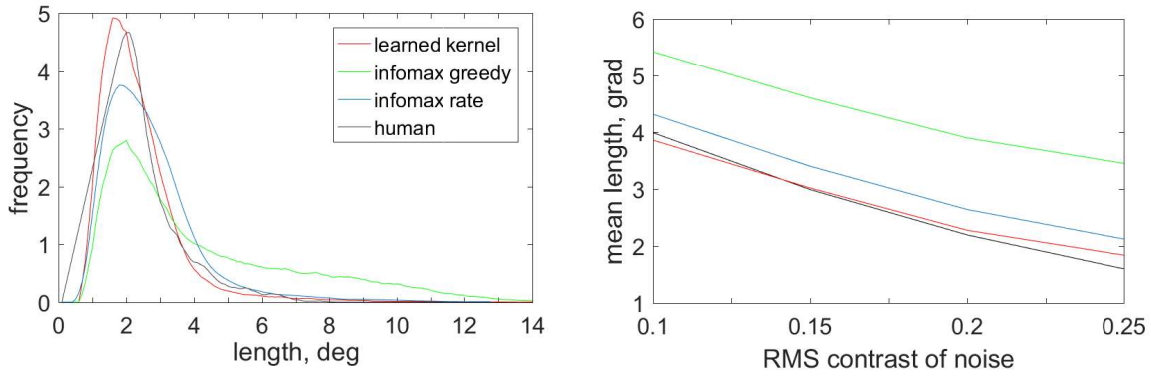


Figure 6: The length distribution of saccadic events (left) for trajectories generated with policies π_0, π_1 and μ_{conv} and human eye-movements corresponding to experimental conditions: $e_n = 0.2, e_t = 0.2$. The distribution function for all policies and human observer exhibits an ascent between 0 deg and maximum around 2deg. The distribution of length corresponding to infomax greedy π_0 stabilizes after 4deg and declines only after 10deg. It is not consistent with length distribution of human saccadic eye-movements, which is concave on interval $[4.0^\circ, 14.0^\circ]$. The mean length of saccades decreases with e_n (right). It's immediate consequence of decrease of width of FPOC with e_n , which defines the area of inhibition from subsequent fixation.

gle between two consequent saccades, and, therefore, can be defined as $\theta_d = \arctan(y_{n+1}/x_{n+1}) - \arctan(y_n/x_n)$, where (y_n, x_n) are coordinates of n th fixation. According to this definition, the movement is related to persistent one if directional angle is close to 0 or 2π . The angles with values close to π correspond to anti-persistent movements.

The distributions of directional angle was calculated for trajectories generated by Markov decision process with policies π_0, π_1 and μ_{conv} . Figure (7)(left) demonstrates directional angle distribution of saccadic events for human observer and simulated trajectories for $e_n = 0.2$ and $e_t = 0.2$. The infomax greedy policy π_0 generates the trajectories with stable anti-persistent movements. The policy π_0 chooses the next fixation location without taking the current location into consideration. Due to inhibitory behavior of infomax, it's much less likely to choose the nearby location instead of remote and relatively unexplored ones. Only geometrical borders limit the choice of the next fixation, which results to fixation on opposite side of visual field (as the most remote point, look at figure (2)).

In contrast, the decision process under learned policy μ tends to preserve the direction of movement. The dynamic of system under policy μ is quite similar to self-avoiding random walk model described in [1]. Due to asymptotical behavior of radial function $R(x)$, the reward gain from remote locations is suppressed, meanwhile the locations, which are already visited, are also inhibited (look at figure (3)). This results in short-range self-avoiding movements, which demonstrate the persistent behavior [37, 1], and, therefore, probability distribution of θ_d is biased towards values 0 or 2π . According to Figure 7 (left), the dynamics under heuristics π_1 is also characterized as persistent random walk. Convolutional policy μ has, in general, a stronger radial ranking of locations than π_1 , which results in shorter range of saccades, and repulsion, caused by inhibition, becomes more relevant. The distribution of average length of saccades depending on θ_d is shown on Figure 7 (right). On average the co-directed movements are shorter than reversal ones for all policies.

In our experiments we discovered that statistical

persistence, in general, depends on visibility of target (on FPOC in simulations). We measured the share of saccades, which retain the direction of previous movement: $\cos(\theta_d) > 0$. This quantity is called "persistence coefficient". The figure 8 demonstrates the dependency of persistence coefficient on RMS contrast of background noise for human observer and simulated trajectories. As it was mentioned previously, the average saccade length is decreasing with growth of RMS contrast (6). Therefore, the linear term (8) in duration of steps becomes less relevant, and decision making becomes more agnostic about temporal costs (closer to information greedy π_0). The decline of persistent coefficient is also a characteristic of human eye movements, which was not covered in previous research.

6. Statistical persistence

In the previous section we have analyzed geometrical persistence of simulated trajectories for different convolutional policies. However, this statistical property doesn't give any insight into long-range correlation in time-series. In this section we show that dynamics under convolutional policies π_0, μ have multifractal behavior, which is similar to that of human eye-movements during visual search [10]. For statistical analysis of simulated trajectories we use multifractal detrended fluctuation analysis (MF-DFA)[38], which is a widely-used method for detection of long-range correlations in stochastic time-series. It has found successful applications in the field of bioinformatics [39, 40], nano and geo-physics [41]. This method is based on approximation of trends in time-series and subtraction of detected trends (detrending) from original data on different scales. The detrending allows to deduct the undesired contribution to long-range correlation, which is result of nonstationarities of physical processes. We use the package provided by Espen Ihlen [42] for all our estimations of generalized Hurst exponent in this section.

6.1. Multifractality of human eye movements

We perform MF-DFA over difference of time series of human gaze positions and in order to com-

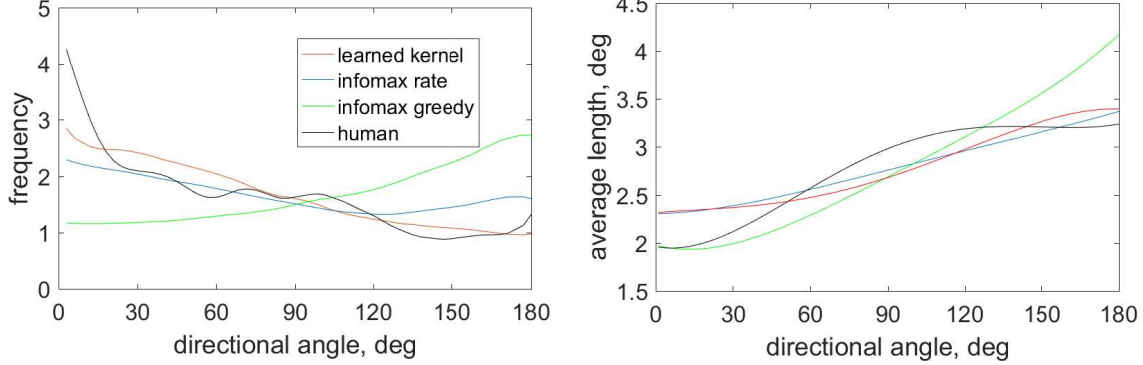


Figure 7: Directional angle distribution (left) and distribution of mean length of saccades to directional angle (right). The infomax greedy policy π_0 generates the trajectories with stable anti-persistent movements (left), with high degree of separation between large and small movements (right). In contrast, the decision process under infomax rate policy π_1 tends to preserve the direction of movement. The dynamics under convolutional function μ_{conv} is also characterized as persistent random walk.

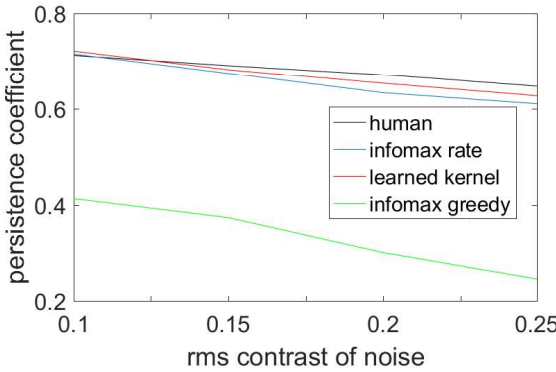


Figure 8: The share of saccades, which retain the direction of previous movement: $\cos(\theta_d) > 0$, is called “persistence coefficient”. This quantity demonstrates dependence on visibility of target. As it was mentioned previously, the average saccade length is decreasing with growth of RMS contrast (6). Therefore, the linear term (8) in duration of steps becomes less relevant, and decision making becomes more agnostic about temporal costs (closer to information greedy π_0). The decline of persistent coefficient is also a characteristic of human eye movements, which was not covered in previous research.

pare the estimated generalized Hurst exponent with simulations. The differentiated time series was estimated from raw data of coordinates of gaze fixations $A = \{(x_1, y_1), \dots (x_N, y_N)\}$ with resolution of 7 ms:

$$\Delta X = \{(x_2 - x_1), \dots (x_N - x_{N-1})\} \quad (24)$$

$$\Delta Y = \{(y_2 - y_1), \dots (y_N - y_{N-1})\} \quad (25)$$

The time series ΔX and ΔY were estimated for each trial with certain experimental conditions and concatenated over all participants. After this, we represent the differentiated time series in the following way: $\Delta X = \{F_1, S_1, \dots, F_{m-1}, S_{m-1}, F_m\}$, where F_i and S_i correspond to sequences of movements during time interval of i -th fixation and saccade respectively [10]. We separate the differentiated time series on fixational and saccadic time series:

$$\Delta X_F = \{F_1, 0 \cdot S_1, \dots, F_{m-1}, 0 \cdot S_{m-1}, F_m\} \quad (26)$$

$$\Delta X_S = \{0 \cdot F_1, S_1, \dots, 0 \cdot F_1, S_{m-1}, 0 \cdot F_1\} \quad (27)$$

Figure 9 demonstrates the scaling of q -order fluctuation function $F_q(s)$ B.4 (left). This graph

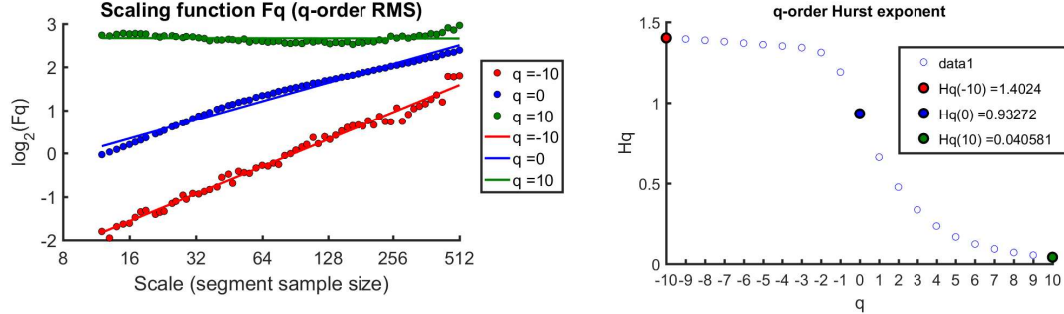


Figure 9: The scaling of q-order fluctuation function $F_q(s)$ (left), and generalized Hurst exponent $H(q)$ (right) computed through linear regression of $\log_2(F_q(s))$. This graph is a result of application of MF-DFA over horizontal differentiated time series ΔX of concatenated human scan-pathes for experimental conditions: $e_t = 0.2$, $e_n = 0.2$. We choose the order of fit function $m = 2$ and set linear space for $s = (s_{min}, s_{min} + \Delta s, \dots, s_{max})$, where $s_{min} = 70 \text{ ms}$, $\Delta s = 7 \text{ ms}$, $s_{max} = 3.5 * 10^3 \text{ ms}$. The red, blue and green lines correspond to linear approximation of function $\log_2(F_q(s))$ for orders $q = \{-10; 0; 10\}$. The scaling of $F_q(s)$ exhibits the crossover on scale $s_{cros} \sim 35$, which corresponds to 245 ms . The crossover separates the “lower” and “upper” regimes mentioned in [10]. The lower regime is related to fixational eye-movements (which is supported by value of crossover scale s_{cros} being close to average fixation duration), and upper regime - to saccadic ones. The crossover in scaling of $F_q(s)$ was observed for all experimental conditions.

is a result of application of MF-DFA over horizontal concatenated differentiated time series ΔX of human scan-pathes for experimental conditions: $e_t = 0.2$, $e_n = 0.2$. We choose the order of fit function $m = 2$ and set linear space: $s = (s_{min}, s_{min} + \Delta s, \dots, s_{max})$, where $s_{min} = 70 \text{ ms}$, $\Delta s = 7 \text{ ms}$, $s_{max} = 3.5 * 10^3 \text{ ms}$. The red, blue and green lines correspond to linear approximation of function $\log_2(F_q(s))$ for orders $q = \{-10; 0; 10\}$. The scaling of $F_q(s)$ exhibits the crossover on scale $s_{cros} \sim 35$, which corresponds to 245 ms . The crossover separates the “lower” and “upper” regimes mentioned in [10]. According to Amor et. al. the crossover is caused by presence of two different generative mechanisms of eye-movements. The lower regime is related to fixational eye-movements (which is supported by value of crossover scale s_{cros} being close to average fixation duration), and upper regime - to saccadic ones. The crossover in scaling of $F_q(s)$ was observed for all experimental conditions. The value of generalized Hurst exponent $H(q)$ (Figure 9 right) is obtained through linear regression of $\log_2(F_q(s))$. Our estimates of $H(q)$ are consistent with the ones of Amor et. al. for both directions and all regimes.

In order to distinguish between two different types of multifractality [38] we calculated $H_{shuf}(q)$ for shuffled differentiated time series. The first type of multifractality is a consequence of broad probability density function for the values of time series. If only multifractality of first type presents in time series, $H(q) = H_{shuf}(q)$. The second type of multifractality is caused by difference in correlation between large and small fluctuations, which is a scenario described in [10]. In this case $H_{shuf}(q) = 0.5$ and $H(q) = 0.5 + H_{corr}(q)$, where $H_{corr}(q)$ is (negative) positive for long-range (anti-)correlation. If both types of multifractality present in time series: $H(q) = H_{shuf}(q) + H_{corr}(q)$.

Figure 10 demonstrates our estimates of Hurst exponent of shuffled time series $H_{shuf}(q)$ (top) and correlational Hurst exponent $H_{corr}(q)$ (bottom) for horizontal (left) and vertical components (right). We estimated both exponents for saccades (green dashed line) and FEM (purple dashed line) in upper and lower regimes of scales respectively. As well as a previous graph 9, this one is a result of application of MF-DFA over concatenated differentiated time series of human eye-movements for experimental conditions: $e_t = 0.2$, $e_n = 0.2$. The behaviour of

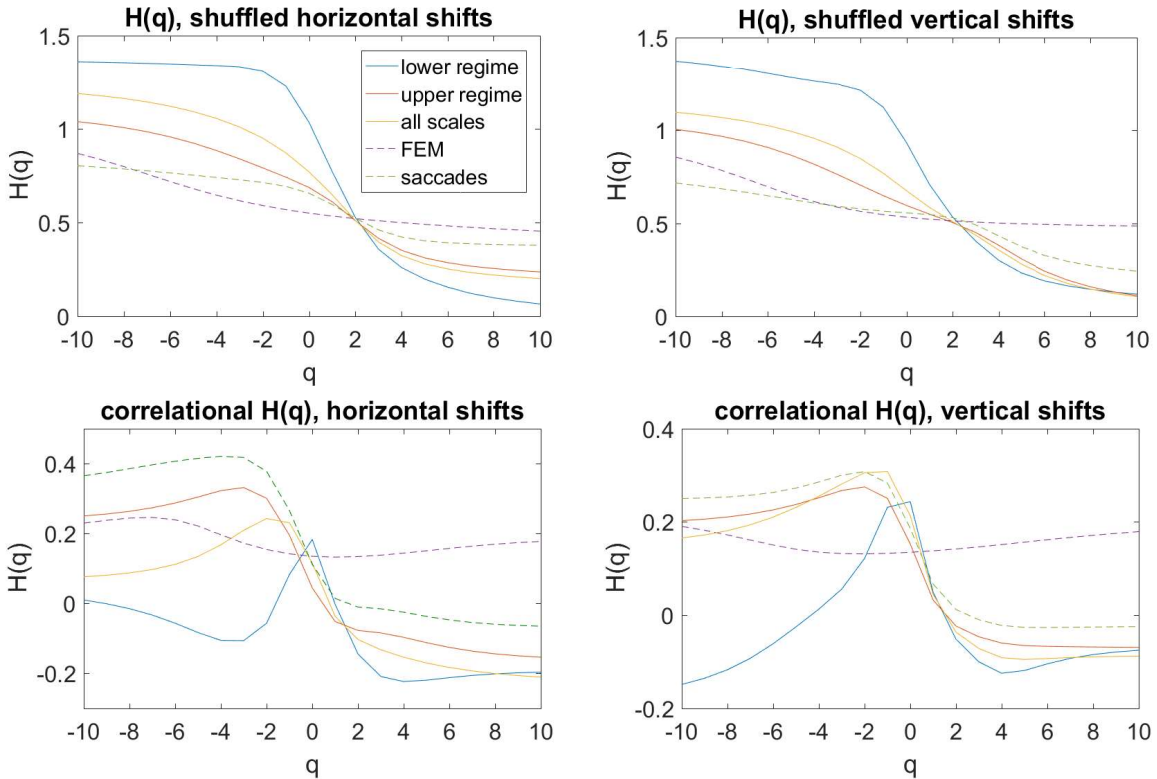


Figure 10: Hurst exponent of shuffled time series $H_{shuf}(q)$ (top) and correlational Hurst exponent $H_{corr}(q)$ (bottom) for horizontal (left) and vertical components (right) of human eye-movements. As well as a previous graph 9, this one is a result of application of MF-DFA over concatenated human scan-paths for experimental conditions: $e_t = 0.2$, $e_n = 0.2$. The behaviour of $H_{shuf}(q)$ for both horizontal and vertical shifts for full scales corresponds to the one mentioned in [38] (eq. 27). We assume that multifractality of first type is caused by asymptomatic behaviour of amplitude distribution of saccades (see figure 6). The difference in long-range correlation of large and small fluctuations is reflected by $H_{corr}(q)$ (figure 10 bottom). Due to the properties of fluctuation function B.4 for positive (negative) q -orders the main contribution are coming from segments containing small (large) fluctuations [38]. The positive (negative) long range correlation ($H_{corr}(q) > 0$) is, therefore, a characteristic of small (large) fluctuations in upper and full scales regimes for both directions. In general, these results are consistent with distribution of average length of saccade to directional angle (see figure 7 right), which also indicates the difference in persistence of large and small saccades.

$H_{shuf}(q)$ for full and saccadic time series in upper regime corresponds to the one mentioned in [38] (eq. 27):

$$h(q) \sim \begin{cases} 1/q & (q > \alpha) \\ 1/\alpha & (q \leq \alpha) \end{cases} \quad (28)$$

with $\alpha \sim 1$. The equation 28 was derived for time series of uncorrelated random values with power law distribution:

$$P = \begin{cases} \alpha x^{-(\alpha+1)} & x \geq 1 \\ 0 & x < 1 \end{cases}. \quad (29)$$

One can see a similarity of function (29) with asymptotical behavior of amplitude distribution of saccadic events for human (see figure 6). The amplitude distribution of saccades demonstrates the power law behavior on the interval $[4.0^\circ, 14.0^\circ]$ with $\alpha \approx 1.5$ for conditions: $e_t = 0.2$, $e_n = 0.2$. Probability distribution function (29) also reflects an absence of saccades with length lower than minimal one. Therefore, the first type multifractality of time series is caused by broad probability distribution of saccade magnitude. In contrast, the behaviour of shuffled fixational time series (FEM) is closer to monofractal one.

The difference in long-range correlation of large and small fluctuations is reflected by $H_{corr}(q)$ (figure 10 bottom). Due to the properties of fluctuation function B.4 for positive (negative) q -orders the main contribution are coming from segments containing large (small) fluctuations [38]. The positive (negative) long range correlation ($H_{corr}(q) > 0$) is, therefore, a characteristic of small (large) fluctuations in upper regime for saccadic and full time series. In general, these results are consistent with distribution of average length of saccade to directional angle (see figure 7 right), which also indicates the difference in persistence of large and small saccades. Therefore, we confirm here that small saccadic eye-movements demonstrate long-range correlations as well as fixational eye-movements.

The time series of FEM demonstrates monofractal behaviour and positive correlations with $H \approx 0.8$ in the lower regime of scales [10]. However, the behaviour of both $H_{corr}(q)$ and $H_{shuf}(q)$ for full time

series in the lower regime indicates the presence of multifractality of both types. At the present moment we have no explanation of the multifractality in lower regime and leave this problem for future work.

6.2. Multifractality of simulated trajectories

We perform MF-DFA over differentiated trajectories generated with PO-MDP under heuristic policies π_0, π_1 and learned policy μ . Before differentiation trajectories were represented as real time sequences with procedure of interpolation Appendix B.2.

We choose the order of fit function $m = 2$ and set linear space for $s = (s_{min}, s_{min} + \Delta s, \dots, s_{max})$, where $s_{min} = 300 \text{ ms}$, $\Delta s = 40 \text{ ms}$, $s_{max} = 3.5 * 10^3 \text{ ms}$. The choice of s_{min} is justified by absence of any movement within fixation interval Θ_{fix} - the system doesn't generate any fluctuations on the time scale s_{max} and below. The model presented here is not devoted to FEM and can't describe the combined movement of both FEM and saccades. The results of our analysis should be compared with the scaling behavior of $F_q(s)$ for human eye-movements on the scales $s \geq 300 \text{ ms}$, which corresponds to upper regime. The choice of $s_{max} = 3.5 * 10^3 \text{ ms}$ corresponds to average length of episode. We assume that there is no correlation between episodes due to random location of first fixation and location of target.

Figure 11 demonstrates the scaling of q -order fluctuation function $F_q(s)$ B.4 for simulated trajectory under infomax rate policy π_1 for conditions: $e_t = 0.2$, $e_n = 0.2$. The red, blue and green lines correspond to linear approximation of function $\log_2(F_q(s))$ for orders $q = \{-10; 0; 10\}$. The scaling of $F_q(s)$ doesn't exhibit the crossover for positive q -orders on interval of scales $[s_{min}, s_{max}]$, however the behavior of $\log_2(F_q(s))$ deviates from linear at large scales $s \sim s_{max}$. The simulations on different grid sizes, which correspond to different average time of task execution, have shown that the interval of linear behavior of $\log_2(F_q(s))$ always coincides with $[s_{min}, s_{max}]$. The asymptotical behavior of fluctuation function at limit $s \rightarrow \infty$ is: $\log_2(F_q(s)) = \text{const}$, which is related to absence

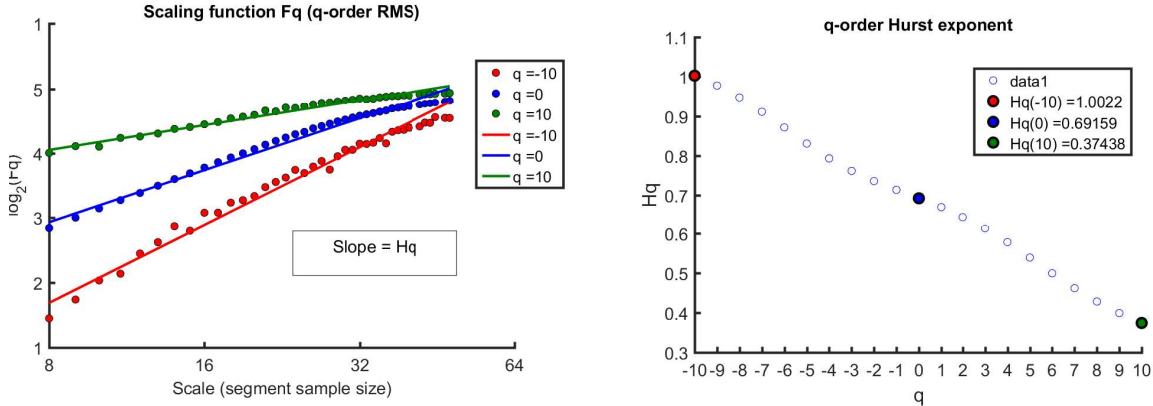


Figure 11: The scaling of q -order fluctuation function $F_q(s)$ (left) estimated for simulated trajectory under infomax rate policy π_1 , and generalized Hurst exponent $H(q)$ (right) computed through linear regression of $\log_2(F_q(s))$. The red, blue and green lines correspond to linear approximation of function $\log_2(F_q(s))$ for orders $q = \{-10; 0; 10\}$. The scaling of $F_q(s)$ doesn't exhibit the crossover for positive q -orders on interval of scales $[s_{min}, s_{max}]$, however the behavior of $\log_2(F_q(s))$ deviates from linear at large scales $s \sim s_{max}$. The simulations on different grid sizes, which correspond to different average time of task execution, have shown that the interval of linear behavior of $\log_2(F_q(s))$ always coincides with $[s_{min}, s_{max}]$. The asymptotical behavior of fluctuation function at limit $s \rightarrow \infty$ is: $\log_2(F_q(s)) = const$, which is related to absence of correlation of fluctuation between episodes. The values of $H(q)$ are different for different orders q and, therefore, the trajectories \bar{A}_{π_1} are multifractal time series.

of correlation of fluctuation between episodes. The scaling of $F_q(s)$ on $[s_{min}, s_{max}]$ is different for different orders q and, therefore, the trajectories \bar{A}_{π_1} are multifractal time series.

Figure 12 demonstrates our estimates of correlational Hurst exponent $H_{corr}(q)$ (left) and Hurst exponent of shuffled time series $H_{shuf}(q)$ of time series simulated under different policies. As well as in the case of human eye-movements, two types of multifractality present in simulated time series. The behavior of $H_{shuf}(q)$ resembles the power-law distribution scenario 28 for all policies. The coefficient $\alpha \approx 1/H(-10)$ is higher for π_1 and μ than the one for infomax greedy π_0 . This is consistent with amplitude distribution 6, which exhibits steeper decline for π_1 and μ in comparison with π_0 .

For both infomax rate π_1 and learned policy μ the correlational Hurst exponent is positive for negative q -orders. This indicates the presence of long-range correlations for small fluctuations. Correlational Hurst exponent changes sign at $q \approx 2$ and $q \approx 4$ for π_1 and μ correspondingly. The large fluc-

tuations are anticorrelated for π_1 and exhibit weak anti-correlation for μ . We observe the last scenario for upper regime of human eye-movements 10, where large fluctuations demonstrate weak anticorrelation in contrary to positively correlated small fluctuations.

6.3. Dependence on visibility

In this section we present comparison of generalized Hurst exponent for human eye-movements in upper regime and simulated trajectories under learned policy. As well as in the case of geometrical persistence, we claim the quantitative properties of statistical persistence depend on visibility of target.

We estimated the correlational Hurst exponent $H_{corr}(q)$ and Hurst exponent of shuffled time series $H_{shuf}(q)$ for differentiated trajectories of human eye-movements for all levels of RMS contrast of background noise: $e_n \in (0.1, 0.15, 0.2, 0.25)$. Figure 13 (left) shows $H_{corr}(q)$ (left) of simulated trajectories (blue) under learned policy μ and correlational Hurst exponent for human eye-movements (pink) averaged over two directions: $H_{corr}(q) =$

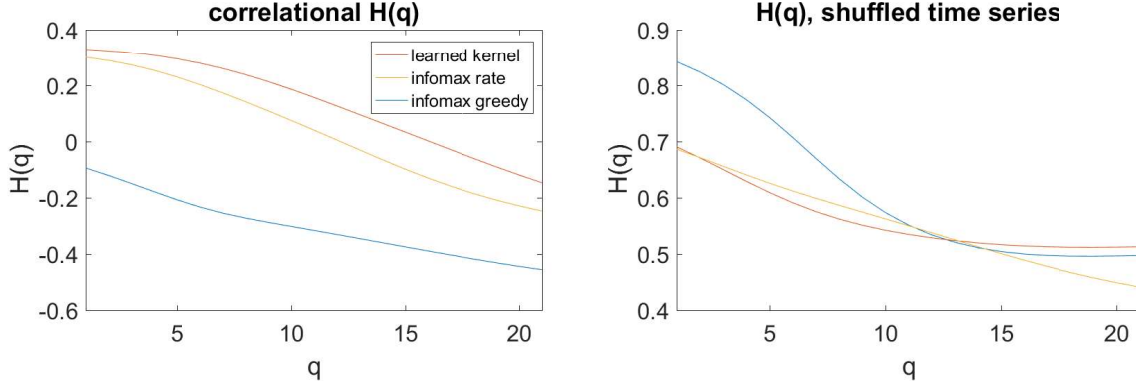


Figure 12: Hurst exponent of shuffled time series $H_{shuf}(q)$ (right) and correlational Hurst exponent $H_{corr}(q)$ (left) of trajectories simulated under different policies. As well as in the case of human eye-movements, two types of multifractality present in simulated time series. The behavior of $H_{shuf}(q)$ resembles the power-law distribution scenario 28 for all policies, which is also characteristic of human eye-movements. The coefficient $\alpha \approx 1/H(-10)$ is higher for π_1 and μ than the one for infomax greedy π_0 . This is consistent with amplitude distribution 6, which exhibits steeper decline for π_1 and μ in comparison with π_0 . As well as in the case of human eye-movements, the first type of multifractality contributes the most to multifractal behaviour of time series. For both infomax rate π_1 and learned policy μ the correlational Hurst exponent is positive for negative q -orders. This indicates the presence of long-range correlations for small fluctuations. Correlational Hurst exponent changes sign at $q \approx 2$ and $q \approx 4$ for π_1 and μ correspondingly. The large fluctuations are anticorrelated for π_1 and exhibit weak anti-correlation for μ . We observe the last scenario for upper regime of human eye-movements 10, where large fluctuations demonstrate weak anti-correlation in contrary to positively correlated small fluctuations.

$(H_{corr}^x(q) + H_{corr}^y(q))/2$ in upper regime. The correlational Hurst exponents for negative q -orders decline with growth of RMS contrast of noise both for human eye-movements and simulated trajectories. This indicates the weakening of correlation between small fluctuations. For positive q -orders the correlational Hurst exponent is less affected by change of visibility of target. The $H_{corr}(q)$ for $q = 10$ stabilized on values -0.2 and -0.12 for human eye-movements and simulated trajectories correspondingly. In general, the correlations weaken with growth of RMS contrast, which is consistent with decline of geometrical persistence 8. The decline of Hurst exponent with increase of difficulty of visual search task was also observed in previous work [12].

The Hurst exponent of shuffled time series (Figure 13 right), as well as correlational Hurst exponent, demonstrates decline with growth of RMS contrast for negative q -orders both for human eye-movements and simulated trajectories. In subsection Appendix B.1 we mentioned that behaviour of

$H_{shuf}(q)$ resembles the one related to time series of random values with power law distribution 29. The average value of this time series equals $1/(\alpha - 1)$ for $\alpha > 1$. The increase of α results both in decrease of average value in time series and decrease of value of $H_{shuf}(q) \sim 1/\alpha$ for $q < 0$. Therefore, the average value in time series and values of $H_{shuf}(q)$ for negative q -orders are correlated in the assumption of power law distribution. Previously we found the decrease of average saccade length with growth of RMS of background noise 6, which is consistent with decrease of values of $H_{shuf}(q)$ for negative q -orders. We assume that this correlation is caused by power law asymptotical behaviour of length distribution of human eye-movements (29).

7. Conclusion

We have presented computational model of ideal observer that both qualitatively and quantitatively describes human visual behaviour during execution of search task. The basis of this model is observer's

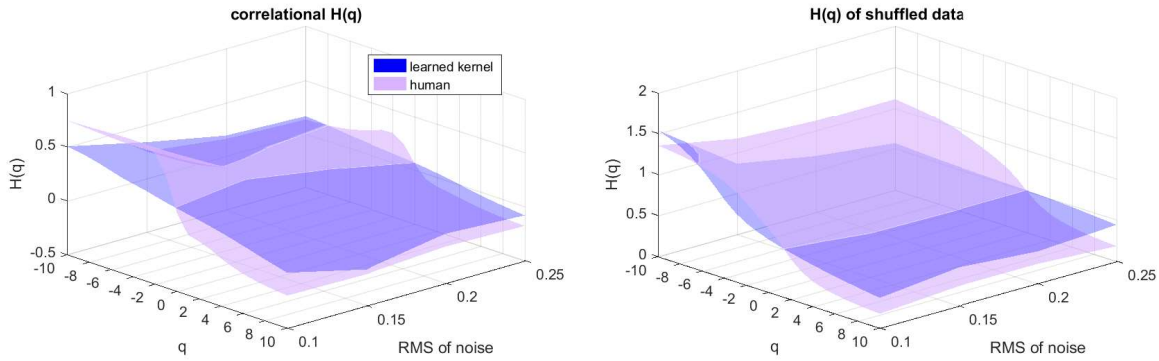


Figure 13: This figure demonstrates $H_{corr}(q)$ (left) of simulated trajectories (blue) under learned policy μ and correlational Hurst exponent for human eye-movements (pink) averaged over two directions: $H_{corr}(q) = (H_{corr}^x(q) + H_{corr}^y(q)) / 2$ in upper regime. The correlational Hurst exponents for negative q -orders declines with growth of RMS contrast of noise both for human eye-movements and simulated trajectories. This indicates the weakening of correlation between small fluctuations. For positive q -orders the correlational Hurst exponent is less affected by change of visibility of target. The $H_{corr}(q)$ for $q = 10$ stabilized on values -0.2 and -0.12 for human eye-movements and simulated trajectories correspondingly. In general, the correlations weaken with growth of RMS contrast, which is consistent with decline of geometrical persistence 8. The decline of Hurst exponent with increase of difficulty of visual search task was also observed in previous work [12]. The Hurst exponent of shuffled time series (right), as well as correlational Hurst exponent, demonstrates decline with growth of RMS contrast for negative q -orders both for human eye-movements and simulated trajectories. In subsection (6.1) we mentioned that behaviour of $H_{shuf}(q)$ resembles the one related to time series of random values with power law distribution 29. The average value of this time series equals $1/(\alpha - 1)$ for $\alpha > 1$. The increase of α results both in decrease of average value in time series and decrease of value of $H_{shuf}(q) \sim 1/\alpha$ for $q < 0$. Therefore, the average value in time series and values of $H_{shuf}(q)$ for negative q -orders are correlated in the assumption of power law distribution. Previously we found the decrease of average saccade length with growth of RMS of background noise 6, which is consistent with decrease of values of $H_{shuf}(q)$ for negative q -orders. We assume that this correlation is caused by power law asymptotical behaviour of length distribution of human eye-movements 29.

representation of constraints of it's own visual and oculomotor systems. We demonstrated that “awareness” of temporal cost and uncertainty of execution of saccades results in dramatical change of basic statistical properties and scaling of simulated time series. Furthermore, it results in observable spiral patterns in trajectories, which is also a characteristic of human eye-movements.

We performed multifractal analysis of our data and discovered the presence of two types of multifractality both in time series of human eye-movements and model simulations. The multifractality caused by broad amplitude distribution of saccades (the first type of multifractality) makes significant contribution to multifractal behaviour of time series, which was not covered in previous work [10]. After estimation of correlational part of Hurst exponent [38] we confirmed the presence of long-range positive correlations of small saccades in upper regime. On the contrary, the large saccades exhibit weak long-range anti-correlations for model simulations and human eye-movements in upper regime. As well as in the case of geometrical persistence, we found that long-range correlations between eye-movements weaken with decline of target's visibility, which is consistent with previous work on this topic [12].

This computational model has significant limitations that will be addressed in future works:

- In this research we focused our attention more on persistence of eye-movements rather than on their spatial distribution. That's why we didn't consider the factors that are not directly related to the trade off between temporal costs and expected information gain. We estimate optimal policy under assumption that visual search process is characterized by shift-rotational symmetry [32], which was not observed in previous work with similar experimental settings [43]. The symmetry of visual search can be broken by angular dependency of FPOC in both cases of normal controls and patients with vision disabilities [44]. We plan to include the angular dependency to radial and smoothing functions of policy (see eq. (21)) in order to consider the

asymmetry of visual field.

- Presented algorithm can not describe the visual behaviour during observation of real world images. It doesn't provide realistic observation model of real objects [32] and doesn't incorporate contextual guidance of eye-movements [45]. Previously it was shown [46] that human observers reduce the area of potential target location through perception of global visual features. Furthermore, during the visual search observers tend to visit the objects related to the target [47]. If we consider this from positions of optimality, information about related objects reduces uncertainty of observer's representation of target. Therefore, it is reasonable to extend the belief state to joint probability distribution in order to describe the inter-relationships between objects. Bayesian inference of target location on tree based contextual model [48] demonstrated significant improvement of object recognition performance. We plan to use this probabilistic model as a prior belief state, which will be updated on each step according to observations of objects.

To sum up, this framework provides elegant explanation of scaling and persistent dynamic of voluntary saccades from optimality point of view. It clearly demonstrates that control models are capable to describe human eye-movements far beyond their basic statistical properties.

8. Acknowledgment

We thank Miles Hansard, Isabelle Mareschal and Ioannis Patras for useful discussions and comments on the manuscript, and Ismail Miflah for help with setting of eye-tracking device. This research was funded by Queen Mary University of London.

Appendix A. Implementation of reinforcement learning algorithms

Appendix A.1. Parametrization of policy

The radial $R(x)$ and smoothing $S(x)$ functions are represented with Fourier-Bessel series:

$$R(x) = \begin{cases} \sum_{\xi=1}^{\Xi} r_{\xi} J_1 \left(\frac{u_{1:\xi}(x-a_{min})}{a_{max}-a_{min}} \right), & a_{min} < x < a_{max} \\ 0, & \text{else} \end{cases} \quad (\text{A.1})$$

$$S(x) = \begin{cases} \sum_{\xi=1}^{\Xi} s_{\xi} J_0 \left(\frac{u_{0:\xi}x}{b} \right), & x < b \\ 0, & \text{else} \end{cases} \quad (\text{A.2})$$

where $u_{i:\xi}$ are zeros of Bessel function of order i and b is the radii of visual field. This representation allows us to control the dimensionality of kernel and to effectively store the policy in memory. The choice of orders ($i = 0, 1$) of Bessel functions in (A.1,A.2) is caused by boundary conditions for radial and smoothing functions: $R(a_{min}) = R(a_{max}) = 0$; $S(b) = 0$. The boundary conditions on radial function forbid the model observer to fixate the same location again $R(0) = 0$ and to make unlikely large saccades $R(a_{max}) = 0$. The condition on smoothing function $S(b) = 0$ corresponds to absence of any information gain from remote locations, and, therefore, their irrelevance to the process of fixation selection. So, the policy $\mu(\vartheta)$ is represented by set of parameters: $\vartheta \equiv (r_{0:\Xi}, s_{0:\Xi})$.

Appendix A.2. REINFORCE

We solve the optimization problem for value function (10) with policy gradient algorithm adopted from [34]. This optimization procedure is represented as iterative process of gradient estimation and update of policy parameters at the end of each training epoch - the sequence of M episodes.

Repeat

1. Perform a training epoch with M episodes and get the sequence of observations, action and costs for each time step t and episode m : $(p_{t,m}, D_{t,m}, L_m)$.
2. Estimate optimal baseline for each gradient element ξ : $b_{\xi} = \frac{\sum_m \left(\sum_t \nabla_{\xi} \log \mu_{\vartheta}(a_{t,m}, p_{t,m}) \right)^2 L_m}{\sum_m \left(\sum_t \nabla_{\xi} \log \mu_{\vartheta}(a_{t,m}, p_{t,m}) \right)^2}$

3. Estimate the gradient for each element: $\eta_{\xi} = \sum_m \left(\sum_t \nabla_{\xi} \log \mu_{\vartheta}(a_{t,m}, p_{t,m}) \right)^2 (b_{\xi} - L_m)$
4. Update policy parameters: $\vartheta \leftarrow \vartheta + \alpha \eta$

until gradient η converges.

Appendix A.3. PGPE

The second approach to optimization problem (10) is parameter exploring policy gradient presented in [31]. As well as in previous section, we estimate the gradient and update the policy parameter at the end of each training epoch. We use symmetric sampling of policy parameters for gradient estimation. At the beginning of each step we generate the perturbation ϵ from normal distribution $N(\mathbf{0}, \mathbf{I}\sigma^2)$ and create symmetric parameter samples $\vartheta^+ = \mu + \epsilon$ and $\vartheta^- = \mu - \epsilon$, where μ is current value of policy parameters for training epoch. Then we simulate one episode for each parameter sample and denote the cost L^+ for episode generated with ϑ^+ , and L^- for ϑ^- correspondingly. At the end of each training epoch policy parameters and variance of distribution of perturbation are updated according to equations:

$$\mu_i = \mu_i + \alpha \sum_{j=1}^M \epsilon_j^i (L_j^- - L_j^+) \quad (\text{A.3})$$

$$\sigma_i = \sigma_i + \alpha \sum_{j=1}^M \left(\frac{(\epsilon_j^i)^2 - \sigma_i^2}{\sigma_i} \right) \left(\langle L \rangle - \frac{L_j^+ + L_j^-}{2} \right) \quad (\text{A.4})$$

where for j th episode ϵ_j^i is perturbation for parameter i and r_j^{\pm} are sampled rewards. The reward baseline is chosen as mean reward for training epoch.

In order to deal with issue of negative estimates of variance we substitute variance with the following continuous function[49]:

$$\sigma^* = \text{expln}(\sigma) = \begin{cases} \exp(\sigma) & \sigma \leq 0 \\ \ln(\sigma + 1) + 1 & \text{else} \end{cases} \quad (\text{A.5})$$

This substitution keeps the variance above zero (exponential) and prevents it from divergence (logarithmic). To use this substitution we need to multiply the update of variance on the derivative of this function [49]:

$$\text{expln}'(\sigma) = \begin{cases} \exp(\sigma) & \sigma \leq 0 \\ \frac{1}{\sigma+1} & \text{else} \end{cases} \quad (\text{A.6})$$

Appendix A.3.1. Convergence of policy gradient

Markov decision process defined by set of dynamic equations (3,4,9,22) was simulated on $N \times N$ grid, which comprises the N^2 possible target locations, where $N = 128$. At the beginning of optimization procedure we pick the policy parameters ϑ randomly from uniform distribution $U(-0.5, 0.5)$ and fix parameter $\lambda = 0.001$. For both algorithms we use the same parametrization of policy. The training epoch for both PGPE and REINFORCE consists of 400 episodes. Learning rate $\alpha = 0.2$ was the same for both algorithms.

Figure A.14 illustrates the performance of two policy gradient methods we used for search of optimal policy for the case of FPOC corresponding to $e_n = 0.15$ and $e_t = 0.2$. Both algorithms used Fourier-Bessel parametrization of policy with dimensionality $\Xi = 45$ for radial and smoothing functions. REINFORCE performed better for all parameter settings. On average, it takes around 50 and 40 learning epochs to converge for REINFORCE and PGPE correspondingly. The choice of dimensionality higher than 45 doesn't improve the performance of both algorithms.

Figure A.15 shows the results of optimization: radial $R(x)$ and smoothing $S(x)$ functions. Both REINFORCE and PGPE provide close estimates of smoothing and radial functions for eccentricity smaller than $\epsilon < 3^\circ$. In order to compare the solution with heuristic policies (13,15), we presented FPOC on the same plot with smoothing function. Smoothing function provided by REINFORCE is monotonously decreasing as well as FPOC, whereas for PGPE we have fluctuating solution with decreasing amplitude of oscillations. The behavior of radial

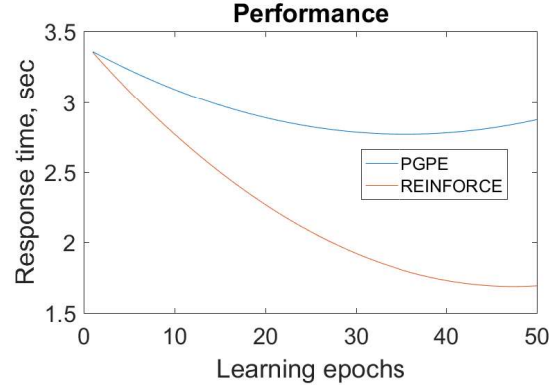


Figure A.14: Performance of parameter exploration policy gradient (PGPE) and episodic REINFORCE with optimal baseline.

function is similar for both solutions, with higher amplitude of oscillations for PGPE solution.

We simulated trajectories for data analysis using the solution provided by REINFORCE due it's better performance than PGPE.

Appendix B. Implementation of MF-DFA

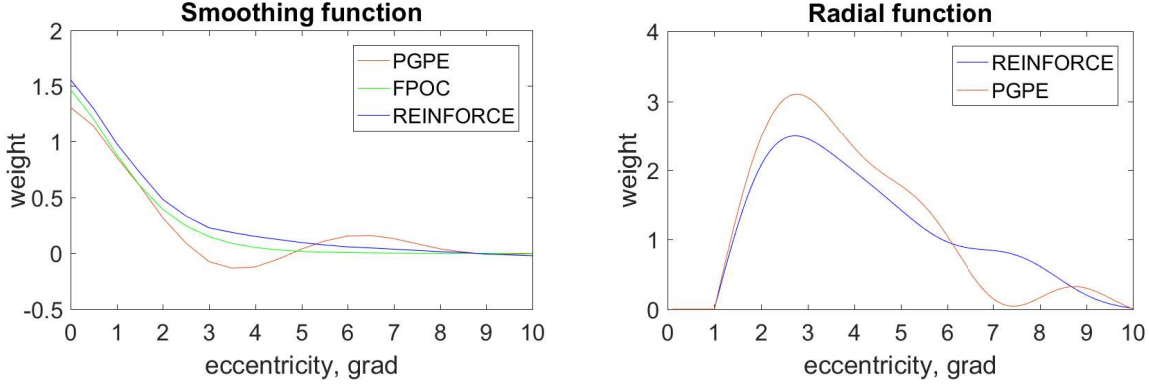
Appendix B.1. Multifractal analysis

In this chapter we discuss the elements of multifractal analysis and details of MF-DFA algorithm used here for calculation of generalized Hurst exponent. All of this section is based on Kantelhardt et al.[38].

The procedure of MF-DFA starts with definition of profile for time series $X = \{x_1, \dots, x_N\}$ with compact support:

$$Y(i) = \sum_{k=1}^i (x_k - \langle x \rangle) \quad (\text{B.1})$$

The profile $Y(i)$ is divided on $N_s \equiv \text{int}(N/s)$ segments, where s is chosen among some linear space $s \in S = \{s_{\min}, s_{\min} + \Delta s, \dots, s_{\max}\}$. The segmentation starts from the beginning of time series, therefore at the end of it there are residual $N \div s$ number of elements. In order to process the residual elements, the segmentation is also performed from the

Figure A.15: Results of optimization: radial $R(x)$ and smoothing $S(x)$ functions.

end of time series. So, at the end of segmentation procedure we have $2N_s$ segments with each s .

The calculation of variance is based on approximation of local trend for each segment $\nu = 1, \dots, N_s$ with polynomial function y_ν . Then, the variance on each segment is calculated as:

$$F^2(\nu, s) = \frac{1}{s} \sum_{i=1}^s \{Y[(\nu - 1)s + i] - y_\nu(i)\}^2 \quad (\text{B.2})$$

for each segment $\nu = 1, \dots, N_s$ and

$$F^2(\nu, s) = \frac{1}{s} \sum_{i=1}^s \{Y[N - (\nu - N_s)s + i] - y_\nu(i)\}^2 \quad (\text{B.3})$$

for $\nu = N_s + 1, \dots, 2N_s$. The order m of polynomial function must satisfy the condition $m \leq s - 2$. The variance over all segments are averaged to obtain the q th order fluctuation function:

$$F_q(s) = \left\{ \frac{1}{2N_s} \sum_{\nu=1}^{2N_s} [F^2(\nu, s)]^{q/2} \right\}^{1/q} \quad (\text{B.4})$$

Where $q \neq 0$. For $q = 0$, the fluctuation function is calculated through a logarithmic averaging procedure[38]:

$$F_q(s) = \exp \left\{ \frac{1}{4N_s} \sum_{\nu=1}^{2N_s} \ln [F^2(\nu, s)] \right\} \quad (\text{B.5})$$

According to properties of q th order fluctuation function [50], the scaling behavior of $F_q(s)$ is governed by generalized Hurst exponent:

$$F_q(s) \sim s^{H(q)} \quad (\text{B.6})$$

The value of $H(q)$ is usually obtained through linear regression of $\log_2(F_q(s))$.

Appendix B.2. Interpolation of simulated trajectories

We perform MF-DFA analysis on magnitude of saccadic events simulated by MDP defined above. Each episode of MDP provides the sequence of vectors of gaze positions: $\mathbf{A}_1, \dots, \mathbf{A}_N$. In order to get the time series of gaze allocation in real time - \bar{A} , we follow the simple procedure of interpolation:

- Calculation of the duration of each time step n with 9, the total time of episode $T = \sum_{i=1}^N \Theta_i$ and start time of each discrete step:

$$T_n = \begin{cases} 0, & \text{if } n = 1 \\ \sum_{i=1}^{n-1} \Theta_i, & \text{if } n > 1 \end{cases} \quad (\text{B.7})$$

- Choice of length of real time sequence $M = 25 * T$, which corresponds to 40 millisecond resolution.
- For each element t of $\bar{\mathbf{A}}$ we define, which discrete time step it belongs: $T_n \leq \frac{t}{25} < T_{n+1}$.
- If time step t of $\bar{\mathbf{A}}_t$ corresponds to fixation during discrete time step $n : \frac{t}{25} - T_n < \Theta_{fix}(n)$, than $\bar{\mathbf{A}}_t = \mathbf{A}_n$. In the other case, if time t corresponds to saccadic movement within discrete time interval n , we have: $\bar{\mathbf{A}}_t = \mathbf{A}_n + \tau_{sac} \frac{\mathbf{A}_{n+1} - \mathbf{A}_n}{|\mathbf{A}_{n+1} - \mathbf{A}_n|} \left(\frac{t}{25} - T_n - \Theta_{fix}(n) \right)$. Therefore, we have defined the function that maps the discrete sequence A to real time sequence \bar{A} .

The real time sequences \bar{A} from 1000 episode corresponding to each policy are merged, and resulting sequences $\bar{A}_\mu, \bar{A}_{\pi_1}, \bar{A}_{\pi_0}$ are analyzed with MF-DFA.

Appendix C. Qualitative analysis

The Figure 4 demonstrated one stimulus image, target object and typical scan-path. Usually, the scan-paths may be divided on three categories, which are defined by number of revolutions of trajectory around the first fixation location and number of intersections. In order to calculate the number of revolutions we have to exclude the first fixation point from the trajectory and start counting from the second fixation location till the final one. After this, the trajectory may be represented by parametric equation in polar coordinates: $r = r(t)$ and $\theta = \theta(t)$, where $r(t)$ and $\theta(t)$ are continuous functions and $t \in [0, 1]$. The number of revolutions is defined as $\text{floor} \left[\frac{|\theta(1) - \theta(0)|}{2\pi} \right]$. If this number is zero the trajectory is called “trivial”, otherwise we call it “spiral” if the trajectory doesn’t have the intersections and “chaotic” in other case (Figure C.16). The trivial trajectories (25% of trials) usually consist of two-three saccades in the same direction and end on target location. Because of randomized location of target for each target, the target may be located quite close to the center of display ($\leq 4 \text{ deg}$). It enables observer to localize the target with low number

of semi-directed eye-movements. The second category are the spiral trajectories (42% of trials), which are shown on Figure C.16. The spiral scan-paths emanate from a central point, moving farther away as they revolve around the center until they stop at target location. No preference in direction of spirals was discovered. The spiral scan-paths consist of consequent saccades with length lower than 4 deg . The angle between saccades is always consistent with geometry of spiral: at the start we may have one-two narrow angles that correspond to higher curvature near the center. In contrast, the second and third loops of spiral consist of saccades with wide directional angles. The third category - chaotic scan-paths (28% of trials) usually behave in the same way as spiral ones, until one or two large saccades intersect the lines of previous saccades.

The motivation behind the spiral trajectories is obvious from positions of optimality. Because of random position of target, observer has to cover the whole visual field with fixations. In order to optimize the speed of search, observer tends to choose the trajectories with smaller length, which correspond to smaller temporal cost. The simplest way to optimize the trajectory in 2D geometry is to deploy it in concentric circles due to highest possible volume/perimeter ratio. The spiral trajectory is the realization of this scenario, which corresponds to our notion of self-similarity of trajectory. We can also observe the spiral scan-paths for simulated trajectories under learned policy μ (Figure C.17). The scan-paths under learned policy consist of small and medium co-directed shifts that result in self-avoiding trajectories, whereas scan-paths generated with greedy infomax policy π_0 are mostly presented by reversal movements. The spiral scan-paths are never generated under π_0 , and all non-trivial trajectories (79%) are chaotic ones. In the same time, the learned policy μ generates 19% of trivial span-paths, 57% of spiral and 24% of chaotic ones.

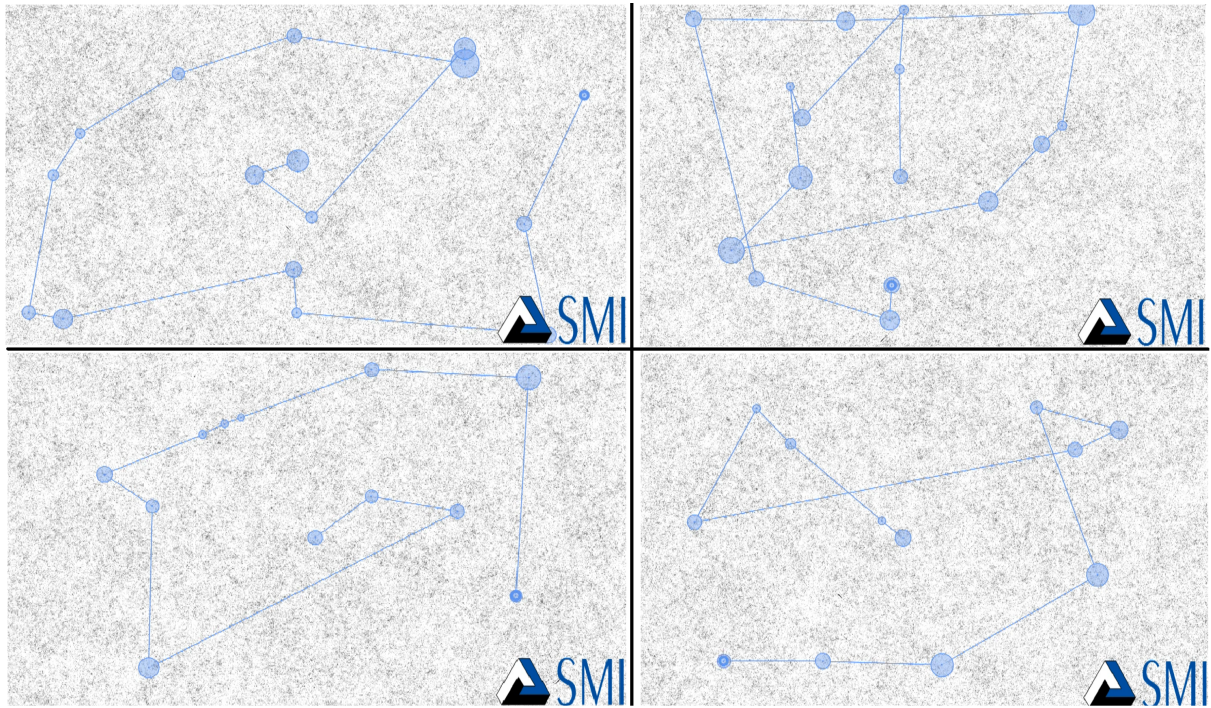


Figure C.16: Spiral (left) and chaotic (right) scan-paths, human eye movements.. The spiral scan-paths emanate from a central point, moving farther away as they revolve around the center until they stop at target location. No preference in direction of spirals was discovered. The spiral scan-paths consist of consequent saccades with length lower than 2deg .

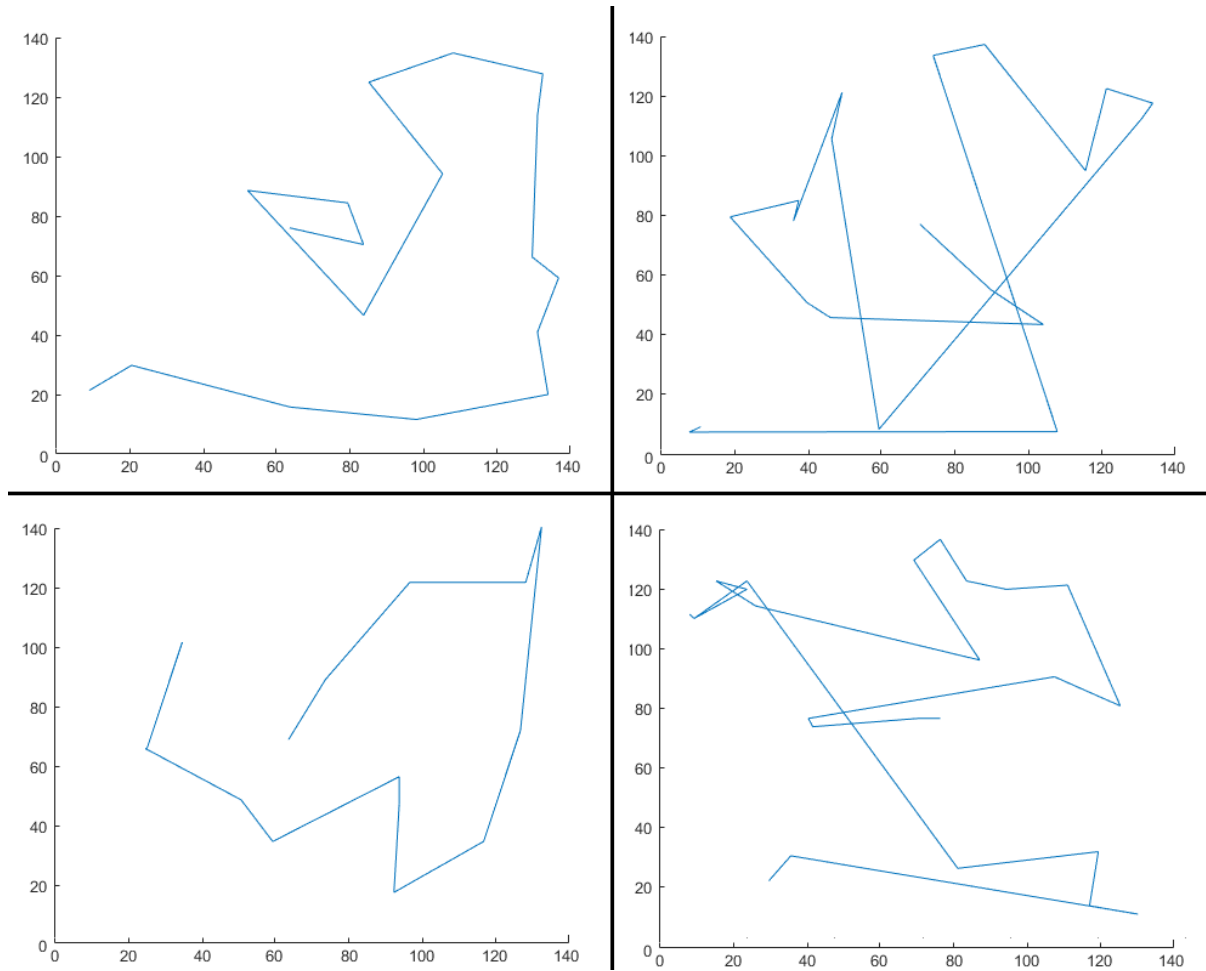


Figure C.17: Spiral and chaotic span-paths corresponding to simulated trajectories under μ (left) and π_0 (right).

References

References

- [1] R. Engbert, K. Mergenthaler, P. Sinn, A. Pikovsky, An integrated model of fixational eye movements and microsaccades, *Proceedings of the National Academy of Sciences* 108 (39) (2011) E765–E770.
- [2] R. Engbert, K. Mergenthaler, Microsaccades are triggered by low retinal image slip, *Proceedings of the National Academy of Sciences* 103 (18) (2006) 7192–7197.
- [3] R. Engbert, R. Kliegl, Microsaccades keep the eyes' balance during fixation, *Psychological Science* 15 (6) (2004) 431–431.
- [4] B. W. Tatler, M. M. Hayhoe, M. F. Land, D. H. Ballard, Eye guidance in natural vision: Reinterpreting salience, *Journal of vision* 11 (5) (2011) 5.
- [5] A. Borji, L. Itti, State-of-the-art in visual attention modeling, *Pattern Analysis and Machine Intelligence, IEEE Transactions on* 35 (1) (2013) 185–207.
- [6] D. H. Ballard, M. M. Hayhoe, Modelling the role of task in the control of gaze, *Visual cognition* 17 (6-7) (2009) 1185–1204.
- [7] H.-k. Ko, M. Poletti, M. Rucci, Microsaccades precisely relocate gaze in a high visual acuity task, *Nature neuroscience* 13 (12) (2010) 1549–1553.
- [8] P. Sinn, R. Engbert, Small saccades versus microsaccades: Experimental distinction and model-based unification, *Vision research* .
- [9] J. Najemnik, W. S. Geisler, Simple summation rule for optimal fixation selection in visual search, *Vision Research* 49 (10) (2009) 1286–1294.
- [10] T. A. Amor, S. D. Reis, D. Campos, H. J. Hermann, J. S. Andrade Jr, Persistence in eye movement during visual search, *Scientific reports* 6.
- [11] J. Najemnik, W. S. Geisler, Optimal eye movement strategies in visual search, *Nature* 434 (7031) (2005) 387–391.
- [12] D. G. Stephen, J. Anastas, Fractal fluctuations in gaze speed visual search, *Attention, Perception, & Psychophysics* 73 (3) (2011) 666–677.
- [13] N. J. Butko, J. R. Movellan, Infomax control of eye movements, *IEEE Transactions on Autonomous Mental Development* 2 (2) (2010) 91–107.
- [14] S. Wallot, C. A. Coey, M. J. Richardson, Cue predictability changes scaling in eye-movement fluctuations, *Attention, Perception, & Psychophysics* 77 (7) (2015) 2169–2180.
- [15] P. Grigolini, G. Aquino, M. Bologna, M. Luković, B. J. West, A theory of 1/f noise in human cognition, *Physica A: Statistical Mechanics and its Applications* 388 (19) (2009) 4192–4204.
- [16] R. J. van Beers, The sources of variability in saccadic eye movements, *The Journal of Neuroscience* 27 (33) (2007) 8757–8770.
- [17] R. Engbert, A. Nuthmann, E. M. Richter, R. Kliegl, SWIFT: a dynamical model of saccade generation during reading., *Psychological review* 112 (4) (2005) 777.
- [18] J. Tian, H. S. Ying, D. S. Zee, Revisiting corrective saccades: role of visual feedback, *Vision research* 89 (2013) 54–64.
- [19] S. P. Lee, J. B. Badler, N. I. Badler, Eyes alive, in: *ACM Transactions on Graphics (TOG)*, vol. 21, ACM, 637–644, 2002.
- [20] A. E. Bartz, Eyemovement latency, duration, and response time as a function of angular displacement., *Journal of Experimental Psychology* 64 (3) (1962) 318.
- [21] T. A. Salthouse, C. L. Ellis, Determinants of eye-fixation duration, *The American journal of psychology* (1980) 207–234.

- [22] S. Lebedev, P. Van Gelder, W. H. Tsui, Square-root relations between main saccadic parameters., *Investigative Ophthalmology & Visual Science* 37 (13) (1996) 2750–2758.
- [23] I. T. C. Hooge, C. J. Erkelens, Control of fixation duration in a simple search task, *Perception & Psychophysics* 58 (7) (1996) 969–976.
- [24] R. Kliegl, A. Nuthmann, R. Engbert, Tracking the mind during reading: the influence of past, present, and future words on fixation durations., *Journal of experimental psychology: General* 135 (1) (2006) 12.
- [25] K. Rayner, G. W. McConkie, S. Ehrlich, Eye movements and integrating information across fixations., *Journal of Experimental Psychology: Human Perception and Performance* 4 (4) (1978) 529.
- [26] H. H. Greene, The control of fixation duration in visual search, *Perception* 35 (3) (2006) 303–315.
- [27] P. J. Unema, S. Pannasch, M. Joos, B. M. Velichkovsky, Time course of information processing during scene perception: The relationship between saccade amplitude and fixation duration, *Visual cognition* 12 (3) (2005) 473–494.
- [28] V. Navalpakkam, C. Koch, A. Rangel, P. Perona, Optimal reward harvesting in complex perceptual environments, *Proceedings of the National Academy of Sciences* 107 (11) (2010) 5232–5237.
- [29] J. Baxter, P. L. Bartlett, Infinite-horizon policy-gradient estimation, *Journal of Artificial Intelligence Research* 15 (2001) 319–350.
- [30] F. Sehnke, A. Graves, C. Osendorfer, J. Schmidhuber, Multimodal parameter-exploring policy gradients, in: *Machine Learning and Applications (ICMLA), 2010 Ninth International Conference on*, IEEE, 113–118, 2010.
- [31] F. Sehnke, C. Osendorfer, T. Rückstieß, A. Graves, J. Peters, J. Schmidhuber, Parameter-exploring policy gradients, *Neural Networks* 23 (4) (2010) 551–559.
- [32] N. J. Butko, J. R. Movellan, I-POMDP: An infomax model of eye movement, in: *2008 7th IEEE International Conference on Development and Learning*, IEEE, 139–144, 2008.
- [33] J. Otero-Millan, X. G. Troncoso, S. L. Macknik, I. Serrano-Pedraza, S. Martinez-Conde, Saccades and microsaccades during visual fixation, exploration, and search: foundations for a common saccadic generator, *Journal of Vision* 8 (14) (2008) 21.
- [34] J. Peters, S. Schaal, Policy gradient methods for robotics, in: *2006 IEEE/RSJ International Conference on Intelligent Robots and Systems*, IEEE, 2219–2225, 2006.
- [35] B. W. Tatler, R. J. Baddeley, B. T. Vincent, The long and the short of it: Spatial statistics at fixation vary with saccade amplitude and task, *Vision research* 46 (12) (2006) 1857–1862.
- [36] M. S. Castelhano, M. L. Mack, J. M. Henderson, Viewing task influences eye movement control during active scene perception, *Journal of Vision* 9 (3) (2009) 6–6.
- [37] S. Isogami, M. Matsushita, Structural and statistical properties of self-avoiding fractional Brownian motion, *Journal of the Physical Society of Japan* 61 (5) (1992) 1445–1448.
- [38] J. W. Kantelhardt, S. A. Zschieghner, E. Koscielny-Bunde, S. Havlin, A. Bunde, H. E. Stanley, Multifractal detrended fluctuation analysis of nonstationary time series, *Physica A: Statistical Mechanics and its Applications* 316 (1) (2002) 87–114.
- [39] A. Rosas, E. Nogueira Jr, J. F. Fontanari, Multifractal analysis of DNA walks and trails, *Physical Review E* 66 (6) (2002) 061906.

[40] S. Dutta, D. Ghosh, S. Chatterjee, Multifractal detrended fluctuation analysis of human gait diseases, *Frontiers in physiology* 4 (2013) 274.

[41] N. Vandewalle, M. Ausloos, M. Houssa, P. Mertens, M. Heyns, Non-Gaussian behavior and anticorrelations in ultrathin gate oxides after soft breakdown, *Applied physics letters* 74 (1999) 1579.

[42] E. A. Ihlen, Introduction to multifractal detrended fluctuation analysis in Matlab, *Fractal Analyses: Statistical And Methodological Innovations And Best Practices* (2012) 97.

[43] J. Najemnik, W. S. Geisler, Eye movement statistics in humans are consistent with an optimal search strategy, *Journal of Vision* 8 (3) (2008) 4–4.

[44] S. Van der Stigchel, R. A. Bethlehem, B. P. Klein, T. T. Berendschot, T. Nijboer, S. O. Du-moulin, Macular degeneration affects eye movement behavior during visual search, *Frontiers in psychology* 4 (2013) 579.

[45] M. B. Neider, G. J. Zelinsky, Scene context guides eye movements during visual search, *Vision research* 46 (5) (2006) 614–621.

[46] A. Torralba, A. Oliva, M. S. Castelhano, J. M. Henderson, Contextual guidance of eye movements and attention in real-world scenes: the role of global features in object search., *Psychological review* 113 (4) (2006) 766.

[47] A. D. Hwang, H.-C. Wang, M. Pomplun, Semantic guidance of eye movements in real-world scenes, *Vision research* 51 (10) (2011) 1192–1205.

[48] M. J. Choi, A. Torralba, A. S. Willsky, A tree-based context model for object recognition, *Pattern Analysis and Machine Intelligence, IEEE Transactions on* 34 (2) (2012) 240–252.

[49] T. Rückstieß, M. Felder, J. Schmidhuber, State-dependent exploration for policy gradient methods, in: *Joint European Conference on Machine Learning and Knowledge Discovery in Databases*, Springer, 234–249, 2008.

[50] H.-O. Peitgen, H. Jürgens, D. Saupe, *Chaos and fractals: new frontiers of science*, Springer Science & Business Media, 2006.

[51] A. Arneodo, E. Bacry, J. Muzy, The thermodynamics of fractals revisited with wavelets, *Physica A: Statistical Mechanics and its Applications* 213 (1) (1995) 232–275.